Brazilian Journal of Geophysics, 44 (2026), 1, 1-14
Brazilian Geophysical Society
ISSN 2764-8044
DOI: 10.22564/brjg.v44i1.00XX

NUMERICAL STABILITY AND DISPERSION ANALYSIS OF FINITE-DIFFERENCE SCHEMES FOR WAVE EQUATION TIME MIGRATION

Alexandre W. Camargo*, Tiago Antonio Alves Coimbra, Jorge Henrique Faccipieri Junior

Universidade Estadual de Campinas - UNICAMP, HPG Lab / CEPETRO, Campinas, SP, Brazil

*Corresponding author e-mail: ale.will.camargo@gmail.com

ABSTRACT. We exploit finite-difference method schemes to solve the wave equation within the migrated time-domain, offering a robust alternative to traditional depth-domain imaging method. While this formulation approximates the acoustic wave equation used in depth models, specific kinematic terms differ. By applying kinematic ray tracing principles to evaluate propagation, we analyze the stability and dispersion of centered and staggered grid schemes. This evaluation is crucial for validating numerical parameters in simulating seis-mic phenomena, bridging the gap between depth and time migration frameworks. Our results indicate that this wave-type behaves numerically similarly to depth-domain models, except for amplitude differences. More-over, the staggered grid scheme superiorly minimizes numerical dispersion and noise. Consequently, this study demonstrates that wave propagation based on plane wave theory and traveltime analysis is highly viable in the time-migrated domain, laying the groundwork for advanced imaging and inversion techniques using two-way equations.

Keywords: wavefront propagation; time-domain imaging; finite-difference method (FDM).

INTRODUCTION

Seismic modeling simulates wave propagation through the Earth's subsurface by approximating complex physics with mathematical models. The acoustic wave equation is a fundamental model for this purpose, typically solved using the finite-difference method (FDM) due to its computational efficiency and ease of implementation. As demonstrated by Kelly et al. (1976) and Liu and Sen (2009, 2011) FDM schemes must strictly adhere to stability and dispersion criteria to ensure numerical solutions of high fidelity.

The precision of FDM modeling depends on these two factors: stability prevents the divergence of numerical errors over time, while dispersion controls the unphysical frequency-dependent velocity variations that can distort waveforms (LeVeque, 2007). In seismic simulations, the acoustic wave equation is standard for depth-domain imaging methods, such as reverse time migration (RTM) (Levin, 1984; Liu et al., 2022) and full-waveform inversion (FWI) (Virieux and Operto, 2009; Gholami et al., 2023), which offer high resolution in complex media but require accurate phase-velocity models.

In contrast, time-domain imaging often relies on traveltime analysis and average velocity models, making it essential for initial seismic processing (Yilmaz, 2001). While traditional time imaging assumes limited lateral velocity variations, modern research focuses on the kinematics of wavefront propagation to handle increased complexity (Schleicher et al., 2008). This often involves kinematic ray tracing and the concept of the image-ray (Hubral, 1977) to facilitate time-to-depth conversion.

A significant advancement in this field was the derivation of the wave equation time migration (WETM) by Fomel and Kaur (2021). Based on plane wave theory and kinematic considerations, WETM governs wave propagation directly within the migrated time-domain. This formulation allows for the adaptation of robust depth-domain tools such as RTM and FWI to time-domain data, potentially improving resolution and velocity estimation (Camargo et al., 2023).

However, while Fomel and Kaur (2021) established the theoretical framework for WETM, the specific numerical challenges regarding its implementation remain underexplored. Unlike the standard acoustic equation, WETM introduces unique terms that affect the grid's numerical behavior. There is a critical gap in understanding how traditional stability and dispersion limits translate to this time-migrated domain, especially when comparing different grid geometries.

In this study, we investigate the numerical stability and dispersion of WETM through Von Neumann analysis. We quantify these effects by varying the approximation orders and comparing centered and staggered grid schemes, a crucial distinction for practical depth and time migration workflows. Our analysis identifies the limitations of the Courant-Friedrichs-Lewy (CFL) condition specific to WETM and provides a comprehensive formula for parameter selection. By establishing these numerical bounds, we demonstrate that WETM is a robust and promising alternative for imaging in geological settings where traditional methods may fail.

METHODS

In order to mathematically describe the concept of the WETM, let us start with the well-known fact that, as already mentioned, most of the experiments in seismic modeling begin with a punctual source in the 2D acoustic wave equation in constant-density media given by

$$\frac{1}{v^2}\frac{\partial^2 U}{\partial t^2} - \mathcal{L}(U) = f(t)\delta(\mathbf{x}-\mathbf{x}_S)\,, \tag{1}$$

where $\mathbf{x} = (x_1, x_2)$ is spatial coordinates, t is the wave propagation time, $v = v(\mathbf{x})$ is the wave velocity propagation, $U = U(\mathbf{x}, t)$ is the scalar wave response, $f(t)$ is the wavelet source, δ is the Dirac's delta, $\mathbf{x}_S = (x_{S1}, x_{S2})$ is the source position, and $\mathcal{L}(\cdot)$ is the Laplacian operator. Moreover, the initial conditions are causal.

Now, to derive the WETM, we employ a coordinate transformation, which in this context is associated with mapping a point in space $\mathbf{x}_0$ to a point in the time-migrated domain by an image-ray path, i.e., $(\xi_0, \tau_0) = (\xi(\mathbf{x}_0), \tau(\mathbf{x}_0))$, as illustrated in Figure 1. Note that the propagation time of the wavefront remains invariant under this transformation; however, it alters its geometry as we change the spatial axes from the depth domain to the time-domain. Additionally, we can observe that the image-ray path is vertically mapped in the transformed configuration during this transformation.

In mathematical terms, we set $U(\mathbf{x}, t) = u(\xi(\mathbf{x}), \tau(\mathbf{x}), t)$ and describe the transformation performed in

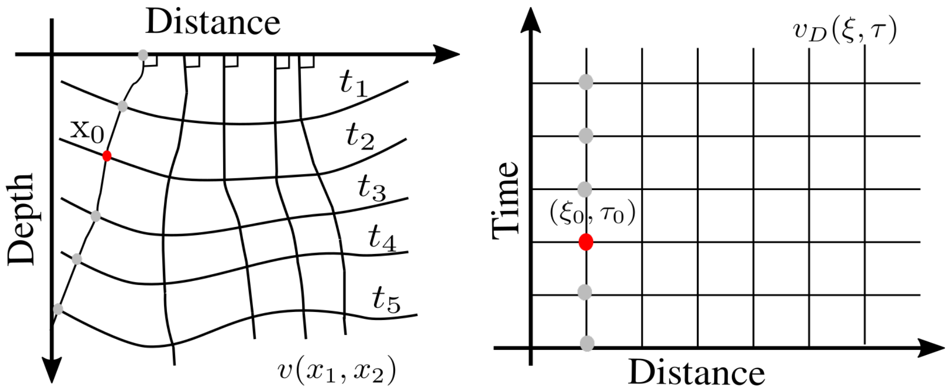

Figure 1: Mapping depth coordinates to an image-ray coordinate. Note that the wavefronts are carried at the same moment t_i for $i = 1, 2, 3, 4, 5$ and started from a plane wave at $x_2 = 0$, where in one medium, we have the velocity v in terms of space, and in the other, a velocity-type v_D is in the medium of the migrated time-domain.

Equation (1) as

$$\begin{aligned} \frac{\partial U}{\partial x_i} &= \frac{\partial u}{\partial \xi}\frac{\partial \xi}{\partial x_i} + \frac{\partial u}{\partial \tau}\frac{\partial \tau}{\partial x_i}\,; \\ \frac{\partial^2 U}{\partial x_i^2} &= \frac{\partial^2 u}{\partial \xi^2}\left(\frac{\partial \xi}{\partial x_i}\right)^2 + \frac{\partial u}{\partial \xi}\frac{\partial^2 \xi}{\partial x_i^2} + \frac{\partial^2 u}{\partial \tau^2}\left(\frac{\partial \tau}{\partial x_i}\right)^2 + \frac{\partial u}{\partial \tau}\frac{\partial^2 \tau}{\partial x_i^2} + 2\frac{\partial^2 u}{\partial \xi \partial \tau}\frac{\partial \xi}{\partial x_i}\frac{\partial \tau}{\partial x_i}\,, \end{aligned} \tag{2}$$

for $i = 1, 2$. Thus, by applying a coordinate transformation in spatial derivatives, we can arrive at the following relationship

$$\mathcal{L}(U) = \frac{\partial^2 u}{\partial \xi^2}\|\nabla \xi\|^2 + \frac{\partial^2 u}{\partial \tau^2}\|\nabla \tau\|^2 + 2\frac{\partial^2 u}{\partial \xi \partial \tau}\nabla \xi \cdot \nabla \tau + \frac{\partial u}{\partial \xi}\mathcal{L}(\xi) + \frac{\partial u}{\partial \tau}\mathcal{L}(\tau)\,. \tag{3}$$

From Cameron et al. (2007), we can represent some terms of Equation (3) concerning the Eikonal equation, the equation of wavefronts geometric spreading, and the relationship between the phase vector and the tangent of wavefronts, i.e.,

$$\begin{cases} \|\nabla \tau\|^2 = \dfrac{1}{v^2(\mathbf{x})}, \\ \|\nabla \xi\|^2 = \dfrac{1}{J^2(\mathbf{x})}, \\ \nabla \xi \cdot \nabla \tau = 0. \end{cases} \tag{4}$$

Furthermore, Cameron et al. (2007) show that the square of Dix's velocity can be given by the ratio of squares of the wave velocity and geometrical spreading J, that is,

$$v_D^2(\xi, \tau) = \frac{v^2(\mathbf{x}(\xi, \tau))}{J^2(\mathbf{x}(\xi, \tau))}. \tag{5}$$

Substituting Equations (4) in (3) and using (5), and assuming that high-frequency components dominate the wavefield in a high-frequency regime, making the second-order terms more significant in describing the wave propagation. Thus, we can remove first-order derivative terms to achieve a more streamlined equation, leaving only second-order derivatives. Therefore, in such a situation, we have

$$\left|\frac{\partial^2 u}{\partial \xi^2} + \frac{1}{v_D^2}\frac{\partial^2 u}{\partial \tau^2}\right| \gg J^2\left|\frac{\partial u}{\partial \xi}\mathcal{L}(\xi) + \frac{\partial u}{\partial \tau}\mathcal{L}(\tau)\right|. \tag{6}$$

Furthermore, the delta function satisfies the following scaling property

$$\delta(\mathbf{x}-\mathbf{x}_S) = \|\nabla\xi\|\|\nabla\tau\|\delta(\xi(\mathbf{x})-\xi_S)\delta(\tau(\mathbf{x})-\tau_S)\,, \tag{7}$$

where $\xi_S = \xi(\mathbf{x}_S)$ and $\tau_S = \tau(\mathbf{x}_S)$. Besides, by construction, $\|\nabla\xi(\mathbf{x}_S)\| = 1/J(\mathbf{x}_S)$ and $\|\nabla\tau(\mathbf{x}_S)\| = 1/v(\mathbf{x}_S)$. Therefore, taking $v_S = v_D(\xi_S, \tau_S)$ and assuming the approximation in Equation (6), from Equations (7) and (5), and also applying Equation (4) in Equation (3), we obtain the WETM as

$$\frac{1}{v_D^2}\left(\frac{\partial^2 u}{\partial t^2} - \frac{\partial^2 u}{\partial \tau^2}\right) - \frac{\partial^2 u}{\partial \xi^2} = \frac{f(t)}{v_S}\delta(\xi-\xi_S)\delta(\tau-\tau_S)\,. \tag{8}$$

Alongside the theory of relating time and depth through a change of coordinates, the work of Ma and Alkhalifah (2013) also tackles the inefficiencies in seismic imaging from different angles. They focus on improving computational efficiency by transforming the vertical axis from depth to vertical traveltime (pseudo-depth), creating a non-orthogonal Riemannian coordinate system that reduces oversampling in deep layers and significantly speeds up the computation of wavefield extrapolations. In contrast, Fomel and Kaur (2021) address the limitations of traditional time migration by formulating WETM through wave propagation in image-ray coordinates, avoiding the use of vertical traveltime approximations, and ensuring geometrical accuracy. WETM approach simplifies the velocity model-building process and enhances image quality, particularly in areas with mild lateral velocity variations. While the pseudo-depth approach centers on reducing computation costs by changing the coordinate system, WETM approach improves the fundamental imaging process by redefining the wave equation in the time migration domain, thus bridging the gap between time and depth migrations.

In summary, Equation (8) describes the mapping of a 2D acoustic equation to a wave-type equation in the time-migrated domain, obtaining a wavefield $u = u(\xi, \tau, t)$. Note that no approximation has been used to obtain the wavefront propagation of Equation (8). In other words, we can say that the content of the kinematics is exact for both equations, see Equations (1) and (8). However, the amplitude is affected because we have neglected the first-order terms, which account for the absorption factor. Finally, as Equation (8) is of the wave-type, we solve it numerically using the FDM scheme considering the two most common approaches that obtain an explicit method: approximating the derivative using the centered and using staggered grid schemes (Moczo et al., 2004). Both of which will be discussed in detail in the following sections.

Centered finite-difference scheme analysis

Hence, employing an explicit high-order FDM on temporal derivative requires a large computer memory allocation and can lead to numerical instability (Liu and Sen, 2009). Therefore, in our analysis, it is sufficient to use a second-order FDM. In mathematical terms, consider the follow numerical discretization as $u_{j,k}^{\ell} = u(\xi_j, \tau_k, t_\ell)$, and its temporal second-order approximation as

$$\frac{\partial^2 u}{\partial t^2} \approx \frac{1}{\Delta t^2}\left[u_{j,k}^{\ell-1} + u_{j,k}^{\ell+1} - 2u_{j,k}^{\ell}\right], \tag{9}$$

where $\xi_j = \xi_0 + j\Delta\xi, \tau_k = \tau_0 + k\Delta\tau$, $t_\ell = t_0 + \ell\Delta t$, $\Delta\xi$, and $\Delta\tau$ are the grid size model and Δt is the time step.

As for ξ and τ derivatives, the most traditional scheme used to solve the acoustic wave equation uses the centered form, which we will follow. However, we will use the higher-order scheme to analyze dispersion and stability. Therefore, we adhere to this formula for the WETM. Thus, using the precision of the operator of order $2M$, i.e.,

$$\begin{aligned}\frac{\partial^2 u}{\partial \xi^2} &\approx \frac{1}{\Delta\xi^2}\sum_{m=1}^{M} c_m\left[u^{\ell}_{j-m,k}+u^{\ell}_{j+m,k}-2u^{\ell}_{j,k}\right],\\ \frac{\partial^2 u}{\partial \tau^2} &\approx \frac{1}{\Delta\tau^2}\sum_{m=1}^{M} c_m\left[u^{\ell}_{j,k-m}+u^{\ell}_{j,k+m}-2u^{\ell}_{j,k}\right],\end{aligned} \tag{10}$$

where c_m, $m = 1,\ldots,M$ are the FDM coefficients based on Taylor expansion (see Fornberg, 1998, which guarantees the consistency of such an approximation), given by

$$c_m = \frac{(-1)^{m+1}}{m^2}\prod_{\substack{1\le p\le M,\\ p\neq m}}\left|\frac{p^2}{p^2-m^2}\right|,\ m = 1,2,\ldots,M; \tag{11}$$

By Duhamel's principle (John, 1978), we can transform Equation (8) in its homogeneous form. Besides, taken $v_{D_{j,k}} = v_D(\xi_j,\tau_k)$, we can apply Equations (9) and (10) in the homogeneous form of Equation (8) in order to obtain

$$\begin{aligned}&\frac{1}{v^2_{D_{j,k}}}\left\{\frac{1}{\Delta t^2}\left[u^{\ell-1}_{j,k}+u^{\ell+1}_{j,k}-2u^{\ell}_{j,k}\right]\right\}-\frac{1}{v^2_{D_{j,k}}}\left\{\frac{1}{\Delta\tau^2}\sum_{m=1}^{M} c_m\left[u^{\ell}_{j,k-m}+u^{\ell}_{j,k+m}-2u^{\ell}_{j,k}\right]\right\}\\ &\quad-\frac{1}{\Delta\xi^2}\sum_{m=1}^{M} c_m\left[u^{\ell}_{j-m,k}+u^{\ell}_{j+m,k}-2u^{\ell}_{j,k}\right]=0.\end{aligned} \tag{12}$$

So, the explicit scheme is given by

$$u^{\ell+1}_{j,k} = 2u^{\ell}_{j,k}-u^{\ell-1}_{j,k}+r^2_{\tau}\sum_{m=1}^{M} c_m\left[u^{\ell}_{j,k-m}+u^{\ell}_{j,k+m}-2u^{\ell}_{j,k}\right]+r^2_{\xi_{j,k}}\sum_{m=1}^{M} c_m\left[u^{\ell}_{j-m,k}+u^{\ell}_{j+m,k}-2u^{\ell}_{j,k}\right], \tag{13}$$

where $r_{\xi_{j,k}} = v_{D_{j,k}}\Delta t/\Delta\xi$, $r_\tau = \Delta t/\Delta\tau$, and

$$\mathcal{C}_{j,k} = \sqrt{r^2_\tau + r^2_{\xi_{j,k}}}, \tag{14}$$

as the Courant number. Besides, the Courant number is an essential metric for the stability of numerical methods used to solve the wave equation. It is closely related to the CFL stability criterion. Furthermore, one necessary condition to ensure the stability of the numerical method (such as the FDM) when solving the WETM is that $\mathcal{C}_{k,j}$ let be less some specific positive number. However, it is important to note that the CFL condition is generally only necessary. If violated, the method does not converge. If satisfied, the method might converge. Still, you need to perform a proper stability analysis to prove the convergence of the method or to determine the adequate stability restrictions.

Numerical analysis of stability and dispersion

The explicit scheme requires certain conditions on both grid and time steps to prevent uncontrolled amplification of numerical errors. To address such conditions and analyze the stability of eq. (13), we apply the Von Neumann analysis (LeVeque, 2007). Therefore, according to the plane wave theory, we can assume that

$$u_{j,k}^{\ell} = [A(\beta)]^{\ell}\, e^{\mathcal{I}(j\beta_\xi \Delta\xi + k\beta_\tau \Delta\tau)}, \tag{15}$$

where

$$\beta_\xi = \frac{\beta}{v_{D^*}}\cos\theta, \quad \beta_\tau = \beta\sin\theta, \tag{16}$$

with θ being the angle of propagation direction of the plane wave propagation, the constant v_{D^*} is a plane wave-type velocity, $\mathcal{I} = \sqrt{-1}$ as the unit imaginary number, and β is an auxiliary frequency dimension parameter. By substituting Equation (15) in Equation (13) with $A = A(\beta)$, we obtain

$$A^2 - g_{j,k}A + 1 = 0, \tag{17}$$

where,

$$\begin{aligned} g_{j,k} = 2 &+ 2\left\{ r_\tau^2 \left[\sum_{m=1}^{M} c_m \left(\cos(m\phi_\tau) - 1\right) \right] \right\} \\ &+ 2\left\{ r_{\xi_{j,k}}^2 \left[\sum_{m=1}^{M} c_m \left(\cos(m\phi_\xi) - 1\right) \right] \right\}, \end{aligned} \tag{18}$$

with $\phi_\tau = \beta_\tau \Delta\tau$, $\phi_\xi = \beta_\xi \Delta\xi$. Isolating the A value, we obtain

$$A = \frac{g_{j,k} \pm \sqrt{g_{j,k}^2 - 4}}{2}. \tag{19}$$

From Equation (15), we have $u_{j,k}^{l+1} = A(\beta)u_{j,k}^{l}$, where the factor $A(\beta)$,represents the amplification factor for the considered method for all β. The amplification factor measures how errors or perturbations in the numerical solution are magnified or attenuated as the solution progresses. Specifically, it indicates how the amplitude of a Fourier mode evolves over each time step (LeVeque, 2007). Therefore, case we set the matrix $U^l = \left[u_{j,k}^{l}\right]$, that implies in $\|U^{l+1}\| \leq |A(\beta)|\|U^l\|$, for all β-value. Based on the Lax–Richtmyer theorem (Lax and Richtmyer, 1956), to ensure the numerical scheme's stability Equation (13), we must demand that $|A| \leq 1$, meaning the numerical errors do not amplify over time. Therefore, satisfying this condition requires $|g_{j,k}| \leq 2$ for all j, k. Furthermore, fixed the values of r_τ and $r_{\xi_{j,k}}$, as the $|g_{j,k}|$-value is maximal when $\phi_\tau = \phi_\xi = \pi$, we can assume that β is the maximum at Nyquist frequency. Thus, such analysis results in

$$\beta_\xi = \frac{\pi}{\Delta\xi} \quad \text{and} \quad \beta_\tau = \frac{\pi}{\Delta\tau}. \tag{20}$$

Therefore, we set $\phi_\tau = \phi_\xi = \pi$ in Equation (18), and considering $\overline{M} = \lfloor M/2 \rfloor$ as the integer part of half of M, we can write

$$
\begin{aligned}
g_{j,k} &= 2 + 2\left\{ r_\tau^2 \left[\sum_{m=1}^{M} c_m \left(\cos(m\pi) - 1\right) \right] \right\} + 2\left\{ r_{\xi_{j,k}}^2 \left[\sum_{m=1}^{M} c_m \left(\cos(m\pi) - 1\right) \right] \right\} \\
&= 2 - 4\left[r_\tau^2 + r_{\xi_{j,k}}^2 \right] \left[\sum_{m=1}^{\overline{M}} c_{2m-1} \right] .
\end{aligned}
\tag{21}
$$

By construction (see, Eq. (11)), we have $c_{2m-1} > 0$. From that, we can conclude the method is stable if

$$
\mathcal{C}_{j,k} \sqrt{\sum_{m=1}^{\overline{M}} c_{2m-1}} \leq 1 \,, \tag{22}
$$

which implies in

$$
\mathcal{C}_{j,k} \leq \mathcal{C}_{\mathrm{MAX}} = \left(\sum_{m=1}^{\overline{M}} c_{2m-1} \right)^{-1/2} . \tag{23}
$$

Figure 2 shows the centered scheme stability region that satisfies inequality given by Equation (23). It can be observed that, as the length increases, this region decreases. This behavior is similar to that observed for the acoustic wave equation, as discussed in Liu and Sen (2009).

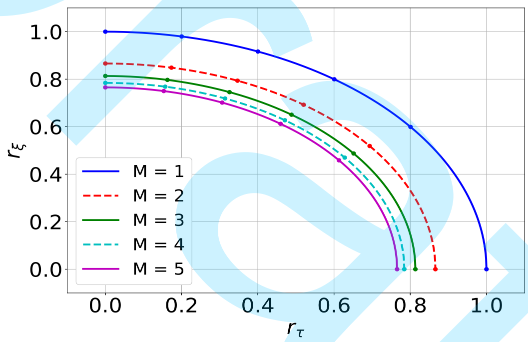

Figure 2: Stability region (inside the lines) based on Courant number for different lengths of the centered scheme.

Now, let us consider the numerical dispersion, which refers to the phenomenon where the numerical solution to the WETM exhibits different propagation velocities for plane waves of different β-values due to the discretization of the equation. Such a phenomenon causes artificial spreading or distortion of wave packets that are not present in the continuous solution. Therefore, numerical dispersion is an inherent artifact of discretizing the continuous situation, leading to different propagation velocities for different β-values in the numerical solution. Understanding and mitigating numerical dispersion is crucial for accurate and stable simulations of this wave-type phenomenon.

As we already mentioned, even ensuring stability, the scheme described by Equation (13) is not free from errors of oscillations in the approximation. An attribution to these oscillations arises from the nonlinearity of the angular frequency with the β values. To analyze this case, we use the plane wave theory again. In mathematical terms,

$$
u(\xi, \tau, t) = u_0 e^{\mathcal{I}(\beta_\xi(\xi-\xi_0)+\beta_\tau(\tau-\tau_0)-\omega(t-t_0))} \,, \tag{24}
$$

where ω is the angular frequency and the parameter u_0 is the wave's amplitude. Therefore, setting the function $u(\xi,\tau,t)$ of Equation (24) in the homogeneous form of Equation (8), we can arrive at

$$\omega^2 = \beta_\tau^2 + v_D^2\beta_\xi^2\,, \tag{25}$$

which using Equation (16), we can conclude

$$\frac{\omega}{\beta} = \pm\sqrt{\sin^2\theta + \left(\frac{v_D}{v_{D^*}}\right)^2\cos^2\theta}\,. \tag{26}$$

However, in situation where $v_D = v_{D^*}$ or $\cos\theta = 0$ such relation became $\beta = \pm\omega$. These oscillations are known as numerical dispersion, and to quantify this numerical phenomenon, we can consider the ratio between these frequencies at each grid point, i.e.,

$$\sigma = \frac{\omega}{\beta}\,. \tag{27}$$

Therefore, there is no dispersion if σ equals one. A large dispersion will occur if σ is far from one. Besides, as already mentioned, $|\beta|$ is equal to $|\omega|$ when $\cos\theta$ in null.

To determine ω, we again use plane wave theory, Equation (24), but now with the time-frequency term, i.e., where the angular frequency dispersion is determined by substituting the harmonic solution applied in scheme (13), so we get

$$[\cos(\omega\Delta t) - 1] = r_\tau^2\sum_{m=1}^{M} c_m\left[\cos(m\phi_\tau) - 1\right] + r_{\xi_{j,k}}^2\sum_{m=1}^{M} c_m\left[\cos(m\phi_\xi) - 1\right]\,, \tag{28}$$

using the identity $2\sin^2(y/2) = 1 - \cos(y)$ and after some rearrangement, we have

$$\omega = \frac{2}{\Delta t}\arcsin\sqrt{r_\tau^2\sum_{m=1}^{M} c_m\sin^2\left(\frac{m\phi_\tau}{2}\right) + r_{\xi_{j,k}}^2\sum_{m=1}^{M} c_m\sin^2\left(\frac{m\phi_\xi}{2}\right)}. \tag{29}$$

Therefore, Substituting the previous result in Equation (27), we have

$$\sigma = \frac{2}{\beta\Delta t}\arcsin\sqrt{r_\tau^2\sum_{m=1}^{M} c_m\sin^2\left(\frac{m\phi_\tau}{2}\right) + r_{\xi_{j,k}}^2\sum_{m=1}^{M} c_m\sin^2\left(\frac{m\phi_\xi}{2}\right)}. \tag{30}$$

Finally, through some manipulations, we obtain

$$\sigma = \frac{\Lambda_{j,k}(\beta)}{\mathcal{C}_{j,k}}\arcsin\sqrt{r_\tau^2\sum_{m=1}^{M} c_m\sin^2\left(\frac{m\phi_\tau}{2}\right) + r_{\xi_{j,k}}^2\sum_{m=1}^{M} c_m\sin^2\left(\frac{m\phi_\xi}{2}\right)}, \tag{31}$$

where

$$\Lambda_{j,k}(\beta) = \frac{2}{\beta}\sqrt{\left(\frac{1}{\Delta\tau}\right)^2 + \left(\frac{v_{D_{j,k}}}{\Delta\xi}\right)^2}\,. \tag{32}$$

To analyze dispersion, let us consider a special case where $\phi_\tau = \phi_\xi = \phi \in [0,\pi]$. In this way, we can rewrite Equation (32) as

$$\Lambda_{j,k} = 2\sqrt{\left(\frac{\sin\theta}{\phi_\tau}\right)^2 + \left(\frac{\cos\theta}{\phi_\xi}\right)^2} = \frac{2}{\phi}\,, \tag{33}$$

and Equation (31) can be written

$$\sigma(\phi) = \frac{2}{\phi \mathcal{C}_{j,k}} \arcsin \sqrt{\mathcal{C}_{j,k}^2 \sum_{m=1}^{M} c_m \sin^2\left(\frac{m\phi}{2}\right)}. \tag{34}$$

To illustrate the dispersion relation, we consider ranges of the maximum value ($\mathcal{C}_{\mathrm{MAX}}$) given by stability condition in Equation (23) by varying the value according to some specific percentages. Figure 3(a) shows the dispersion for 20% of $\mathcal{C}_{\mathrm{MAX}}$, where it is observed that the higher the order of approximation of the scheme, the lower the dispersion. Considering values of 40%, 80% and 100% of $\mathcal{C}_{\mathrm{MAX}}$, the behavior is maintained with increases in dispersion, as we can see in Figure 3(b), Figure 3(c) and Figure 3(d), respectively. Assuming an acceptable dispersion of 10%, we have a wide range of ϕ for $M > 1$. Another interesting point is that the second-order scheme ($M = 1$) would be dispersion-free for the maximum value in this case.

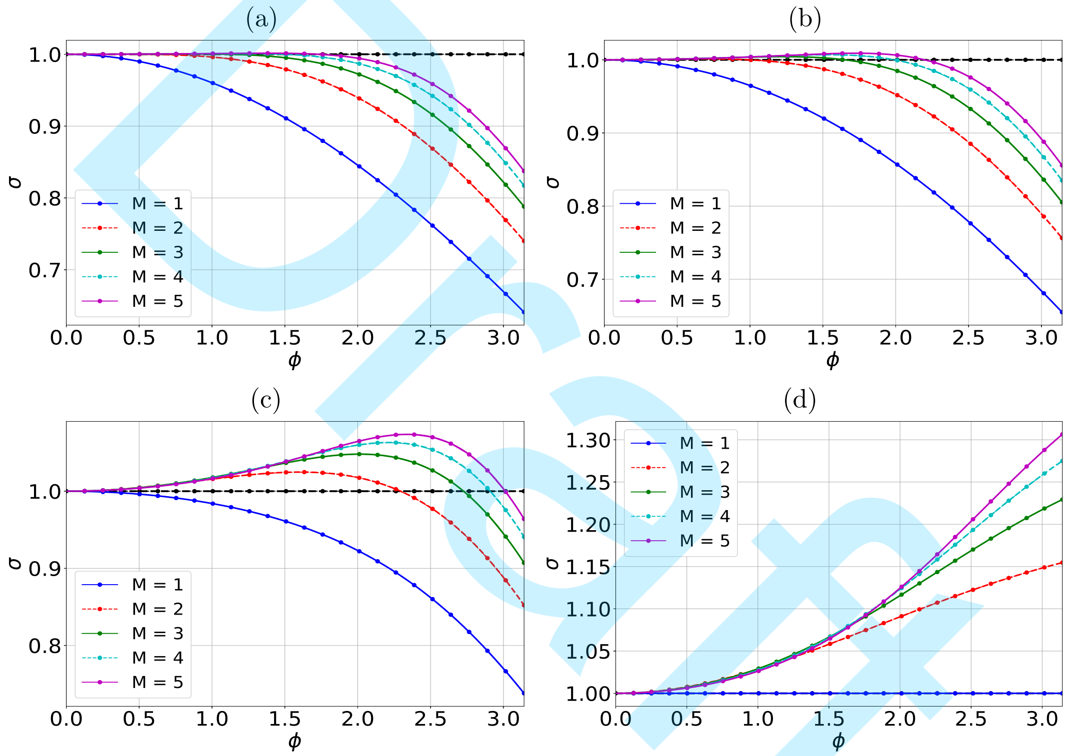

Figure 3: Dispersion curve for different operator lengths using the centered FDM scheme (a) 20% of $\mathcal{C}_{\mathrm{MAX}}$; (b) 40% of $\mathcal{C}_{\mathrm{MAX}}$; (c) 80% of $\mathcal{C}_{\mathrm{MAX}}$; (d) 100% of $\mathcal{C}_{\mathrm{MAX}}$.

Staggered grid scheme analysis

Besides the centered scheme, the staggered grid scheme is widely used for achieving more optimized approximation coefficients, such as Holberg (1987); Liu (2014); Zhang et al. (2023).

So, for the temporal derivative t part, we use the same order of approximation given by Equation (9). For the derivatives of the time-migrated domain, we will use the same $2M$th-order approximation, where the first derivative is given by

$$\frac{\partial u}{\partial \xi} \approx \frac{1}{\Delta\xi} \sum_{m=1}^{M} a_m \left(u^{\ell}_{j+m-1/2,k} - u^{\ell}_{j-m+1/2,k}\right), \quad \frac{\partial u}{\partial \tau} \approx \frac{1}{\Delta\tau} \sum_{m=1}^{M} a_m \left(u^{\ell}_{j,k+m-1/2} - u^{\ell}_{j,k-m+1/2}\right), \tag{35}$$

where

$$a_m = \frac{(-1)^{m+1}}{2m-1} \prod_{\substack{1\le p\le M,\\ p\neq m}} \left| \frac{(2p-1)^2}{(2p-1)^2-(2m-1)^2} \right|, \; m = 1,2,\ldots,M. \tag{36}$$

Applying Equation (35) twice to get the second-order derivative approximation, we can obtain the following scheme

$$\begin{aligned} u_{j,k}^{\ell+1} &= 2u_{j,k}^{\ell} - u_{j,k}^{\ell-1} \\ &+ r_\tau^2 \sum_{m=1}^{M}\sum_{n=1}^{M} a_m a_n \left[\left(u_{j,k+m+n-1}^{\ell} - u_{j,k-m+n}^{\ell} \right) - \left(u_{j,k+m-n}^{\ell} - u_{j,k-m-n+1}^{\ell} \right) \right] \\ &+ r_{\xi_{j,k}}^2 \sum_{m=1}^{M}\sum_{n=1}^{M} a_m a_n \left[\left(u_{j+m+n-1,k}^{\ell} - u_{j-m+n,k}^{\ell} \right) - \left(u_{j+m-n,k}^{\ell} - u_{j-m-n+1,k}^{\ell} \right) \right]. \end{aligned} \tag{37}$$

Similarly to the centered scheme, we can apply the Von Neumann analysis as in Equation (17) to obtain

$$g_{j,k} = 2 - 2r_\tau^2 \left(\sum_{m=1}^{M} a_m \sin(m-0.5)\phi_\tau \right)^2 - 2r_{\xi_{j,k}}^2 \left(\sum_{m=1}^{M} a_m \sin(m-0.5)\phi_\xi \right)^2. \tag{38}$$

To ensure stability, consider the maximum Nyquist frequency, that is $\phi_\tau = \phi_\xi = \pi$, thus $\sin(m-0.5)\pi = (-1)^{m+1}$ since the odd terms are positive and the even terms are negative according to the coefficient formula (36), stability can be expressed

$$\mathcal{C}_{j,k} \left(\sum_{m=1}^{M} |a_m| \right) \le \sqrt{2}, \tag{39}$$

which implies in

$$\mathcal{C}_{j,k} \le \mathcal{C}_{\mathrm{MAX}} = \sqrt{2} \left(\sum_{m=1}^{M} |a_m| \right)^{-1}. \tag{40}$$

In the case of dispersion analysis, we have

$$\sigma = \frac{\Lambda_{j,k}(\beta)}{\mathcal{C}_{j,k}} \arcsin \left(\left(r_\tau \sum_{m=1}^{M} a_m \sin(m-0.5)\phi_\tau \right)^2 + \left(r_{\xi_{j,k}} \sum_{m=1}^{M} a_m \sin(m-0.5)\phi_\xi \right)^2 \right)^{1/2}. \tag{41}$$

For special case when $\phi_\tau = \phi_\xi = \phi$, we have

$$\sigma(\phi) = \frac{2}{\phi \mathcal{C}_{j,k}} \arcsin \left[\mathcal{C}_{j,k} \sum_{m=1}^{M} a_m \sin(m-0.5)\phi \right]. \tag{42}$$

Figure 4 shows the stability region varying for the staggered grid scheme. Compared to the centered one (Fig. 2), we see that the region is more expanded, i.e., in the direction of stability, there are more points that guarantee the method's stability. From another perspective, we can compare in Figure 5 the $\mathcal{C}_{\mathrm{MAX}}$ values for each length, observing that the staggered grid has a higher limiting value than the centered scheme.

For the dispersion observed in Figure 6(a), 6(b), 6(c) and 6(d) for 20%, 40%, 80%, and 100% of $\mathcal{C}_{\mathrm{MAX}}$, respectively, the behavior is quite similar to that observed in the centered scheme. However, for the 20% and 40% ranges of $\mathcal{C}_{\mathrm{MAX}}$, the staggered scheme proves to be less dispersive than the centered scheme. For the 80% and 100% ranges, the variation in dispersion is very similar up to an interval of $\pi/2$; beyond this point, the centered scheme becomes more favorable.

Choice step-size grid

The accuracy and calculation amount of FDM modeling directly depends on the FDM stencil size, which determines the length of $\Delta\xi$ and $\Delta\tau$, and the grid size of the time step, which determines the length of Δt.

Increasing the FDN stencil size increases the modeling calculation amount and improves the accuracy. We can

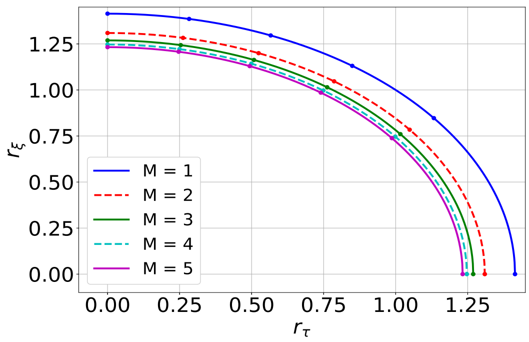

Figure 4: Stability region (inside the lines) based on Courant number for different lengths of the staggered scheme.

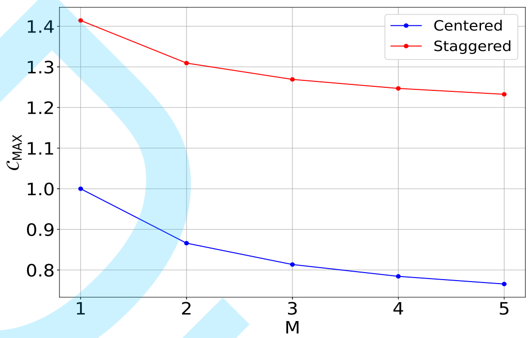

Figure 5: Maximum value for stability condition considering the centered and staggered schemes.

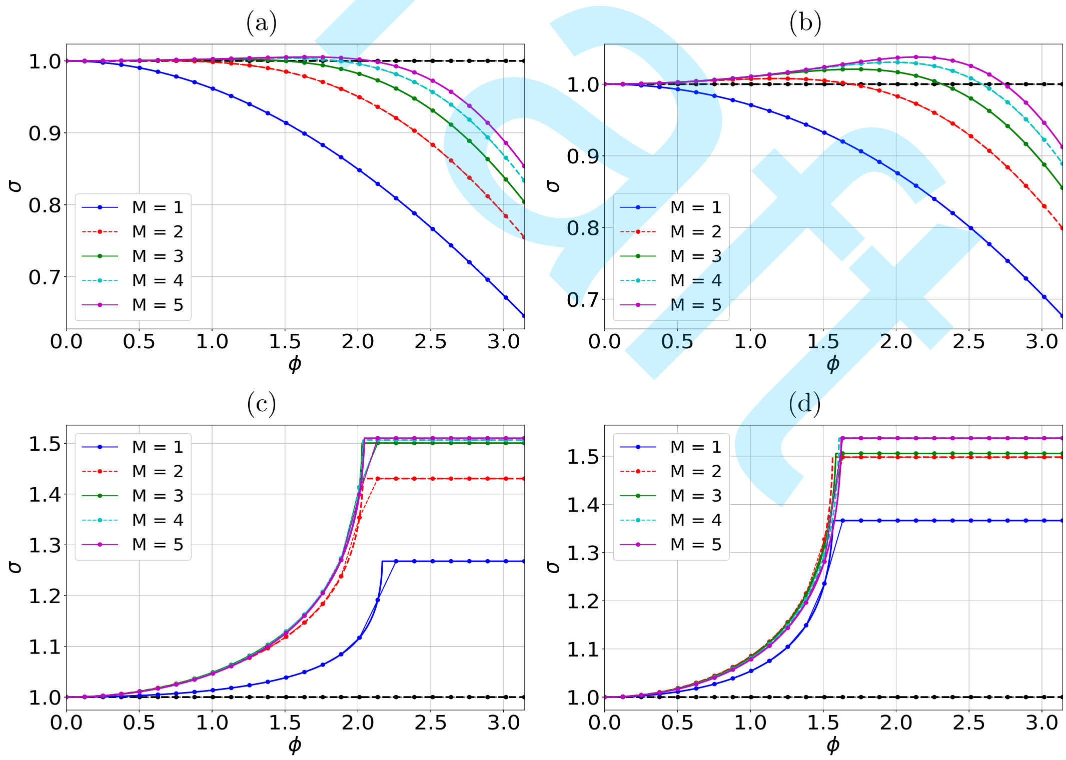

Figure 6: Dispersion curve for different operator lengths using the staggered FDM scheme (a) 20% of $\mathcal{C}_{\mathrm{MAX}}$; (b) 40% of $\mathcal{C}_{\mathrm{MAX}}$; (c) 80% of $\mathcal{C}_{\mathrm{MAX}}$; (d) 100% of $\mathcal{C}_{\mathrm{MAX}}$.

simultaneously increase the FDM stencil size and reduce the grid size of the time step to maintain modeling accuracy. Therefore, there is a tradeoff between the accuracy and the calculation amount for a given modeling accuracy, which depends on the FDM stencil size and grid size of the time step. We can find an optimal FDM stencil size that provides the minimum calculation amount. Therefore, based on the stability and dispersion analysis for acoustic wave equation found in Camargo and Santos (2013), we derive a criterion for selecting the step-size for $\Delta\xi$, $\Delta\tau$, and consequently Δt.

From the numerical dispersion analysis, we can choose a suitable ϕ_* from Equations. (34) and (42). Accordingly, we can bound the FDM stencil size for $\Delta\xi$ and $\Delta\tau$ obeying

$$\Delta\xi \leq \frac{\phi_* v_D^-}{\omega_+}\,, \quad \text{and} \quad \Delta\tau \leq \frac{\phi_*}{\omega_+}\,, \tag{43}$$

where $v_D^- = \min_{j,k}\{v_{D_{j,k}}\}$, ω_+ is the maximum angular frequency of the source $f(t)$. Since chosen $\Delta\xi_*$, $\Delta\tau_*$ based on Equation (43), Δt can be chosen by

$$\Delta t \leq \frac{\mathcal{C}_{\text{MAX}}}{\sqrt{\left(\dfrac{v_D^+}{\Delta\xi_*}\right)^2 + \left(\dfrac{1}{\Delta\tau_*}\right)^2}}\,, \tag{44}$$

with $v_D^+ = \max_{j,k}\{v_{D_{j,k}}\}$.

RESULTS

In order to analyze the stability and dispersion criteria, we conducted two synthetic experiments to check the WETM behavior for simulating waves in a one-way traveltime model in the migrated time-domain. The first simulation is a medium consisting of only two horizontal plane layers. It is a medium with little difficulty for FDM simulation with well-separated events. Therefore, the idea of such a simple model is to analyze the phenomena of interest in a qualitative (visual) way. The second has greater complexity, where we use a modified version of Marmousi2 (Martin et al., 2002) as a benchmark for the qualitative analysis. In the experiments, the point source term is the Ricker pulse. Additionally, we employed the implementation with Convolutional Perfectly Matched Layer (CPML) absorbing boundaries (Komatitsch and Martin, 2007) using a 51-point window.

Reflector model

Figure 7 illustrates the reflector model in the one-way traveltime migrated time-domain. Concerning the numerical parameters, we use a spatial-time discretization of $\Delta\xi = 0.01$ [km] $\Delta\tau = 0.004$ [s], and a peak angular frequency of Ricker pulse was set at 125 [rad/s]. These parameters were chosen based on a $\phi_* = 2.2$ value and limiting the maximum angular frequency to 314 [rad/s].

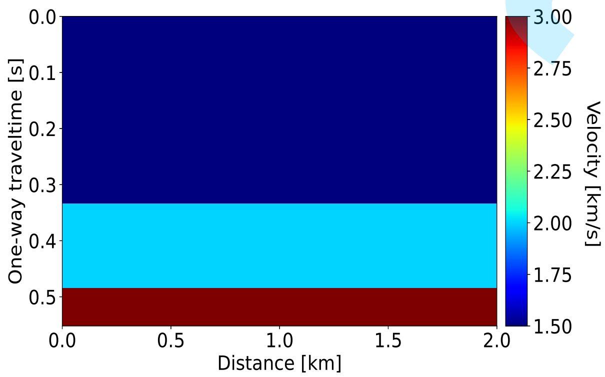

Figure 7: Reflector model velocity wave in the migrated time-domain $v_0 = 1.5$ [km/s], $v_1 = 2.0$ [km/s] and $v_2 = 3$ [km/s] are layers velocities.

We set the parameters $\Delta\xi$ and $\Delta\tau$ to assess the influence of the numerical schemes based on all values of M analyzed.

Additionally, for the centered and staggered FDM schemes, we chose Δt to be equal to 40% of C_{MAX} for each M value. In this instance, the WETM response was measured for a 0.5 [km] source with three receivers at 0.55 [km], 0.85 [km], and 1.05 [km].

Therefore, for $M = 1$, the choice of Δt was 0.001 [s] for the centered scheme and 0.0014 [s] for the staggered scheme. This is consistent with the stability equation's two roots squared factor. The response is illustrated in Figure 8, where the odd indices represent the centered scheme and the even ones are the staggered scheme. The two schemes exhibit dispersion, with the signals being practically identical. It can thus be concluded that the choice of scheme does not influence the signal response. However, the staggered scheme offers an advantage in allowing fewer points per time than the centered scheme. This implies a reduction in computational cost and storage requirements.

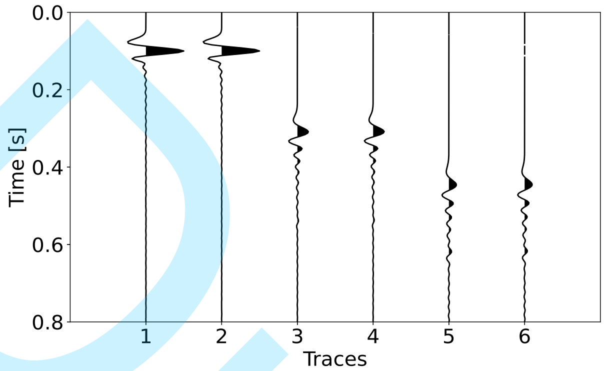

Figure 8: Comparison of traces for each numerical scheme for $M = 1$. Odd numbers indicate the centered scheme, while even numbers indicate the staggered scheme. It was considered $\Delta t = 0.001$ [s] for centered scheme and $\Delta t = 0.0014$ [s] for staggered scheme.

Considering the centered and staggered schems, we obtain for $M = 2$, $\Delta t = 0.009$ [s] (centered), $\Delta t = 0.0013$ [s] (staggered); and for $M = 5$, $\Delta t = 0.008$ [s] (centered), $\Delta t = 0.0012$ [s] (staggered). The traces are presented in Figures 9 and 10. As observed previously, the scheme choice has no significant impact, and the numerical dispersion decreases as the value of M increases.

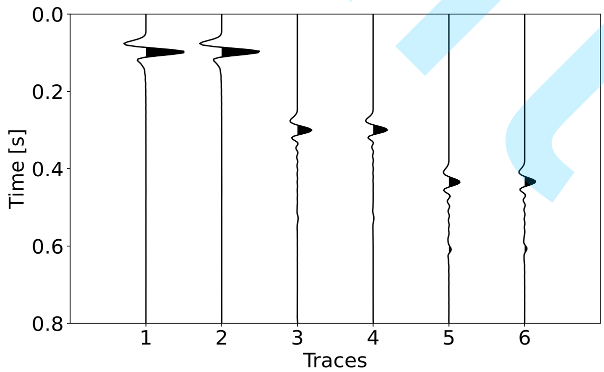

Figure 9: Comparison of traces for each numerical scheme for $M = 2$. Odd numbers indicate the centered scheme, while even numbers indicate the staggered scheme. It was considered $\Delta t = 0.0009$ [s] for centered scheme and $\Delta t = 0.0013$ [s] for staggered scheme.

Finally, in the concluding test, we conducted a seismic experiment. The results, depicted in Figure 11(a) for the acoustic wave equation and Figure 11(b) for the WETM, demonstrate identical kinematics in the responses. The only discernible difference lies in the amplitude.

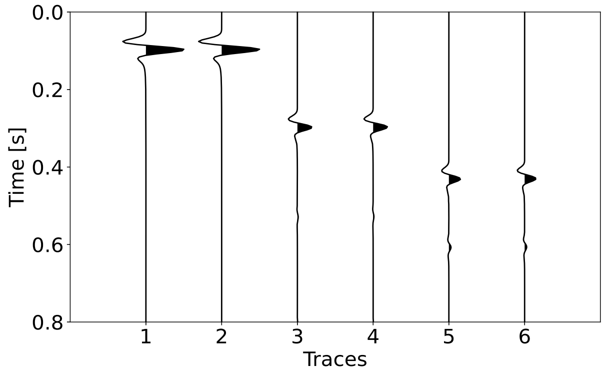

Figure 10: Comparison of traces for each numerical scheme for $M = 5$. Odd numbers indicate the centered scheme, while even numbers indicate the staggered scheme. It was considered $\Delta t = 0.0008$ [s] for centered scheme and $\Delta t = 0.0012$ [s] for staggered scheme.

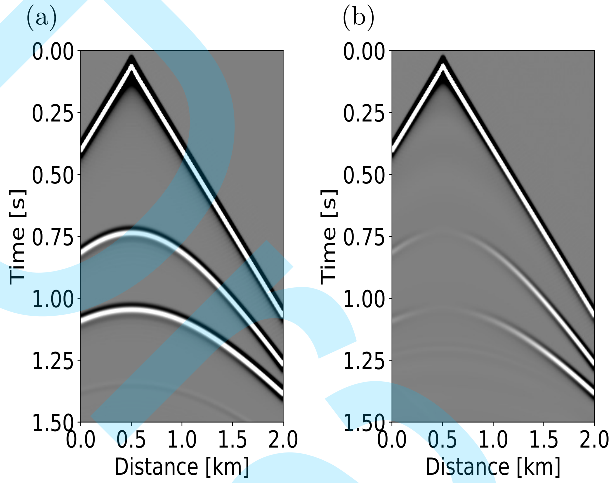

Figure 11: Common shot record positioned at $(0.5, 0)$ [km] for the reflector model in the following domains: (a) Depth; (b) One-way traveltime.

Marmousi2 model

This second experiment considers a modified version of the Marmousi2 model, chosen for its increased complexity. The velocity model, depicted in terms of traveltime in Figure 12, has dimensions of 681×273. For the propagation simulation, a Ricker pulse with a peak angular frequency of 125 [rad/s].

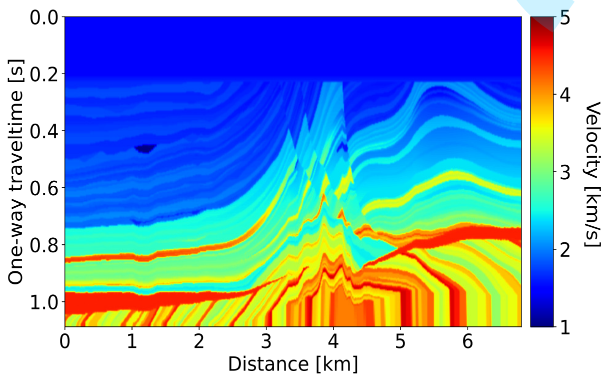

Figure 12: Marmousi2 velocity wave in the time-domain.

In this particular experiment, we set the numerical parameters to $\Delta\xi = 0.01$ [km], $\Delta\tau = 0.004$ [s] and $\Delta t = 0.001$ [s].

Theses values were derived from a stability factor of $\phi_* = 2.4$, utilizing 40% of C_{MAX} threshold to evaluate how operator length influences image integrity. Figures 13(a)–(c) ilustrate modelling snapshots at the $t = 0.15$ [s] for approximation order $M = 1, 2, 5$, respectively. While all cases satisfy the stability condition, numerical dispersion is significantly more pronounced in the second-order FDM scheme ($M = 1$). In contrast, the fourth-order ($M = 2$) and tenth-order ($M = 5$) schemes effectively mitigate these artifacts, demonstrating that higher-order operators are essential for preserving wavefront.

As propagation progresses, the interaction between dispersion and geological reflections becomes more complex. In Figure 14(a), the second-order scheme exhibits strong dispersive reverberations associated with the direct wave. However, for higher-order schemes (Figures 14(b) and (c)), these effects are considerably reduced, though subtle dispersive tails can sometimes be masked by high-amplitude reflection events. This behavior confirms that the WETM, despite operating in the migrated time-domain, faces numerical challenges analogous to those encountered in traditional depth-domain wave equations.

Detailed reflections shown in Figure 15 further validate these observations. The low-order operator (Fig. 15(a)) remains plagued by dispersion-induced noise, whereas the tenth-order operator (Fig. 15(c)) provides a high-fidelity representation of the subsurface kinematics. Furthermore, the integration of CPML absorbing boundaries proved sufficient to suppress boundary reflections, ensuring that the analyzed snapshots are free from edge-related artifacts.

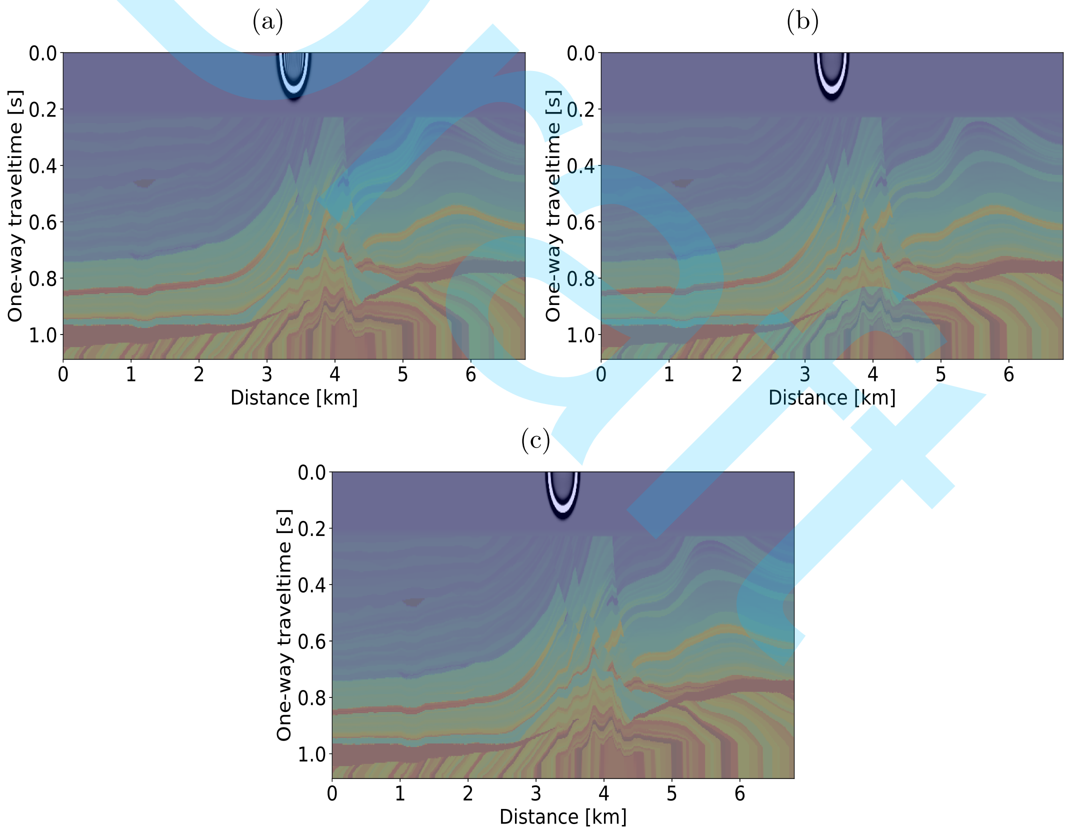

Figure 13: Modeled snapshot at time $t = 0.15$ [s] depicting wave propagation in the Marmousi2 model: (a) $M = 1$; (b) $M = 2$; (c) $M = 5$.

The influence of the choice affect the amplitude of the frequency spectrum; the greater the numerical errors, the more significant the frequency contribution near the band between 63 [rad/s] and 314 [rad/s]. Figure 16(a) compares the true Ricker source with the numerical result, while Figure 16(b) displays the absolute error. The low error indicates that the high-order operator provides a closer approximation to the true value.

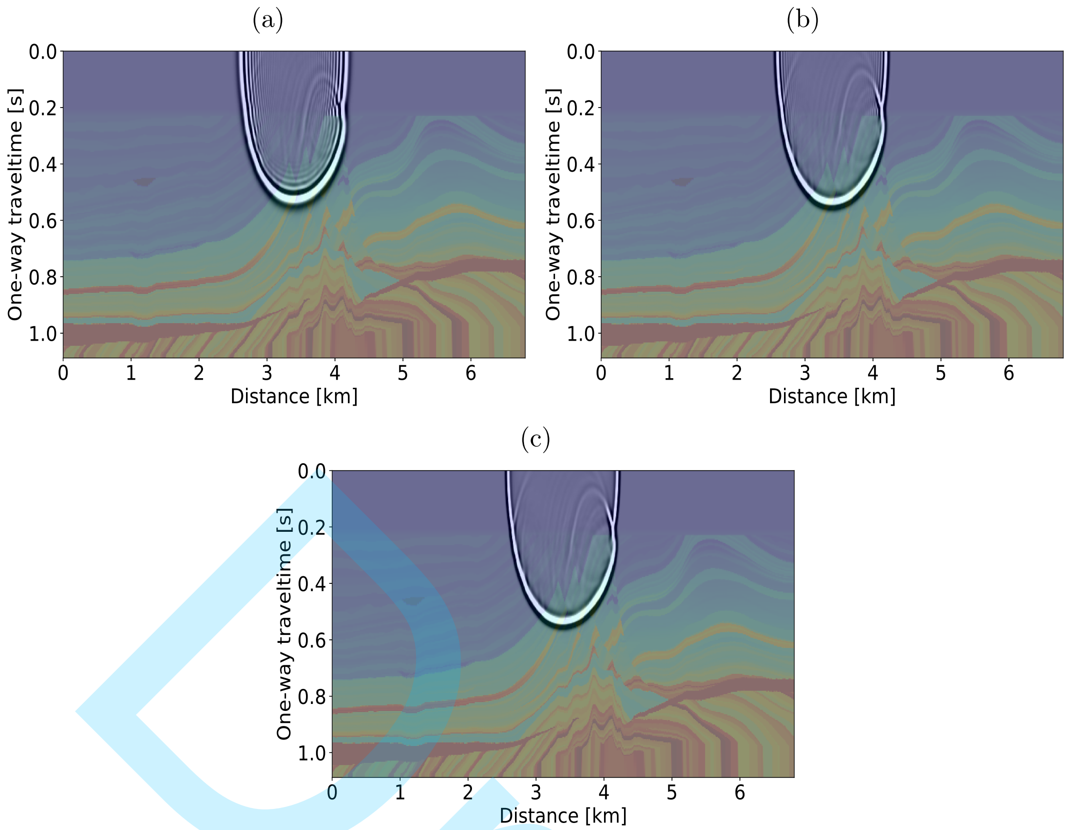

Figure 14: Modeled snapshot at time $t = 0.55$ [s] depicting wave propagation in the Marmousi2 model: (a) $M = 1$; (b) $M = 2$; (c) $M = 5$.

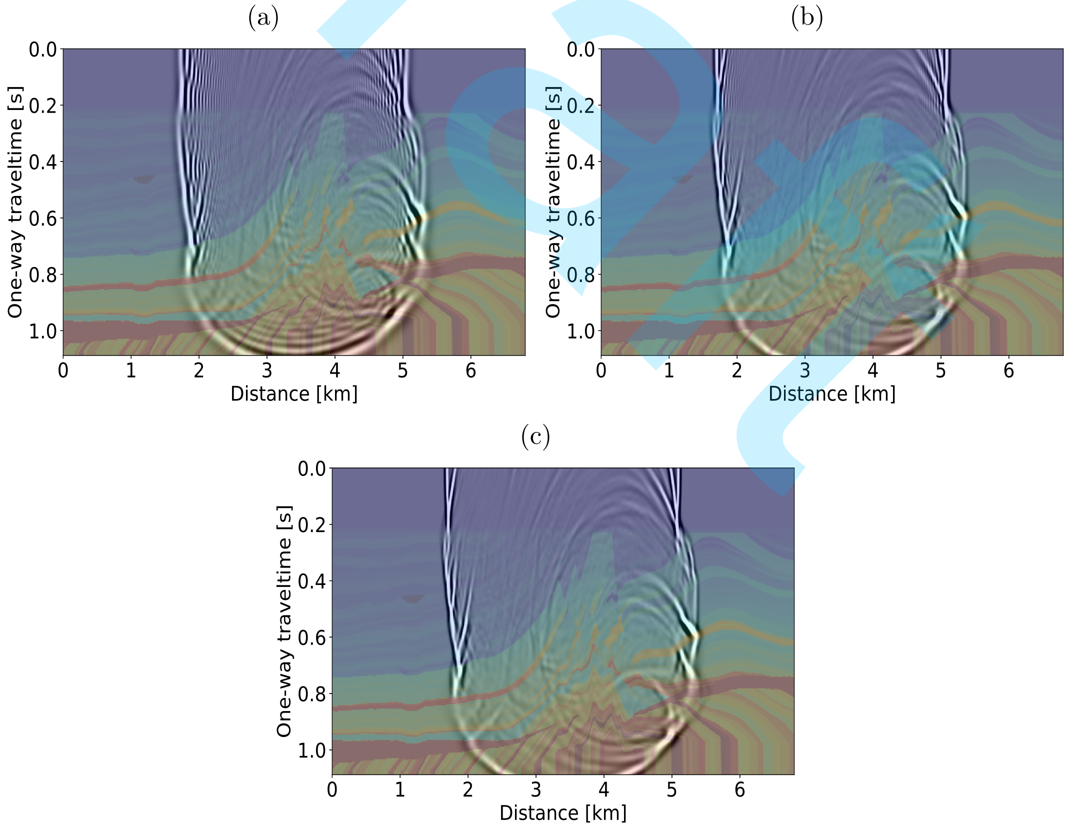

Figure 15: Modeled snapshot at time $t = 1.05$ [s] depicting wave propagation in the Marmousi2 model: (a) $M = 1$; (b) $M = 2$; (c) $M = 5$.

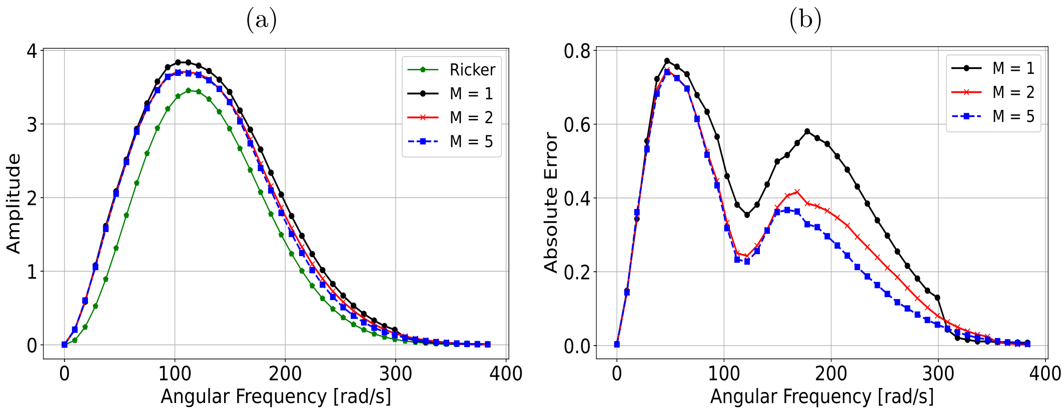

Figure 16: Frequency analysis in different M-values: (a) Spectrum frequency; (b) Absolute error.

CONCLUSION

This study established the stability and dispersion criteria for solving the Wave Equation in Time Migration (WETM) using centered and staggered-grid finite-difference schemes. While the choice of scheme does not fundamentally alter the numerical solution, the staggered grid demonstrates a superior stability region, offering greater flexibility in temporal step-size selection. Our analysis reveals that WETM yields high accuracy with negligible dispersion, provided the numerical parameters are appropriately tuned. Furthermore, the observed amplitude decay along the image-ray path, a result of the equation's theoretical formulation, promotes a more balanced energy distribution across other propagation directions.

By utilizing a wave-equation-based approach rather than traditional Kirchhoff or paraxial-ray theories, we significantly expand the range of complex models processable in the time domain. WETM is particularly effective in geological settings with moderate lateral velocity variations, where it honors wave physics without the smoothing requirements typically imposed on ray-based methods to maintain stability. Ultimately, the robust numerical framework presented here facilitates the integration of WETM into high-resolution workflows such as RTM and FWI, providing a powerful alternative for advanced subsurface characterization and time-domain imaging.

REFERENCES

Camargo, A. W., T. A. Coimbra, and J. H. Faccipieri, 2023, Time-lapse analysis using the wave-equation time migration: 18th International Congress of the Brazilian Geophysical Society, SBGf, Rio de Janeiro, RJ, Brazil., 1–6.

Camargo, A. W., and L. T. Santos, 2013, Finite-differences with adaptive spatial operator for the 1D wave equation: Dispersion and stability analysis: 13th International Congress of the Brazilian Geophysical Society, SBGf, Rio de Janeiro, RJ, Brazil., 1–3. doi: 10.1190/sbgf2013-284.

Cameron, M. K., S. B. Fomel, and J. A. Sethian, 2007, Seismic velocity estimation from time migration: Inverse Problems, **23**, 1329–1369, doi: 10.1088/0266-5611/23/4/001.

Fomel, S., and H. Kaur, 2021, Wave-equation time migration: Geophysics, **86**, S103–S111, doi: 10.1190/geo2019-0822.1.

Fornberg, B., 1998, Classroom note: Calculation of weights in finite difference formulas: SIAM Review, **40**, 685–691, doi: 10.1137/S0036144596322507.

Gholami, A., H. S. Aghamiry, and S. Operto, 2023, Multiplier waveform inversion: A reduced-space full-waveform inversion by the method of multipliers: Geophysics, **88**, R339–R354, doi: 10.1190/geo2022-0343.1.

Holberg, O., 1987, Computational aspects of the choice of operator and sampling interval for numerical differentiation in large-scale simulation of wave phenomena: Geophysical Prospecting, **35**, 629–655, doi: 10.1111/j.1365-

2478.1987.tb00841.x.

Hubral, P., 1977, Time migration – Some ray theoretical aspects: Geophysical Prospecting, **25**, 738–745, doi: 10.1111/j.1365-2478.1977.tb01200.x.

John, F., 1978, Partial differential equations, softcover reprint of the original 3rd edition ed. Applied Mathematical Sciences (Switzerland): Springer. doi:10.1007/978-1-4684-0059-5.

Kelly, K. R., R. W. Ward, S. Treitel, and R. M. Alford, 1976, Synthetic seismograms: A finite-difference approach: Geophysics, **41**, 2–27, doi: 10.1190/1.1440605.

Komatitsch, D., and R. Martin, 2007, An unsplit convolutional perfectly matched layer improved at grazing incidence for the seismic wave equation: Geophysics, **72**, SM155–SM167, doi: 10.1190/1.2757586.

Lax, P. D., and R. D. Richtmyer, 1956, Survey of the stability of linear finite difference equations: Communications on Pure and Applied Mathematics, **9**, 267–293, doi: 10.1002/cpa.3160090206.

LeVeque, R. J., 2007, Finite difference methods for ordinary and partial differential equations: Steady-state and time-dependent problems: Society for Industrial and Applied Mathematics. Philadelphia, PA, USA. 342 pp.

Levin, S. A., 1984, Principle of reverse-time migration: Geophysics, **49**, 581–583, doi: 10.1190/1.1441693.

Liu, Y., 2014, Optimal staggered-grid finite-difference schemes based on least-squares for wave equation modelling: Geophysical Journal International, **197**, 1033–1047, doi: 10.1093/gji/ggu032.

Liu, Y., W. Liu, Z. Wu, and J. Yang, 2022, Reverse time migration with an exact two-way illumination compensation: Geophysics, **87**, S53–S62, doi: 10.1190/geo2020-0815.1.

Liu, Y., and M. K. Sen, 2009, A new time–space domain high-order finite-difference method for the acoustic wave equation: Journal of Computational Physics, **228**, 8779–8806, doi: 10.1016/j.jcp.2009.08.027.

Liu, Y., and M. K. Sen, 2011, Finite-difference modeling with adaptive variable-length spatial operators: Geophysics, **76**, T79–T89, doi: 10.1190/1.3587223.

Ma, X., and T. Alkhalifah, 2013, Wavefield extrapolation in pseudodepth domain: Geophysics, **78**, S81–S91, doi: 10.1190/geo2012-0237.1.

Martin, G. S., K. J. Marfurt, and S. Larsen, 2002, Marmousi-2: An updated model for the investigation of AVO in structurally complex areas: SEG Technical Program Expanded Abstracts 2002, Society of Exploration Geophysicists, 1–4. doi: 10.1190/1.1817083.

Moczo, P., J. Kristek, and L. Halada, 2004, The finite-difference method for seismologists. an introduction.: Comenius University Bratislava.

Schleicher, J., J. C. Costa, and A. Novais, 2008, Time-migration velocity analysis by image-wave propagation of common-image gathers: Geophysics, **73**, VE161–VE171, doi: 10.1190/1.2968952.

Virieux, J., and S. Operto, 2009, An overview of full-waveform inversion in exploration geophysics: Geophysics, **74**, WCC1–WCC26, doi: 10.1190/1.3238367.

Yilmaz, O., 2001, Seismic data analysis: Processing, inversion and interpretation of seismic data: Society of Exploration Geophysicists.

Zhang, C., L. Fan, G. Chen, and X. Zeng, 2023, Efficient temporal high-order staggered-grid scheme with a dispersion-relation-preserving method for the scalar wave modeling: Frontiers in Earth Science, **11**, doi: 10.3389/feart.2023.1141220.

Camargo, A. W.: Conceptualization, Writing – original draft, Writing – review & editing; **Coimbra, T. A. A.**: Conceptualization, Writing – original draft, Writing – review & editing; **Faccipieri Junior, J. H.**: Conceptualization, Writing – original draft, Writing – review & editing.